# Ultra-high-voltage Ni-rich layered cathodes in practical Li metal batteries enabled by a sulfonamide-based electrolyte

Weijiang Xue [1], Mingjun Huang [2], Yutao Li[3], Yun Guang Zhu[4], Rui Gao[1], Xianghui Xiao[5], Wenxu Zhang[2], Sipei Li[4], Guiyin Xu [1], Yang Yu[6], Peng Li[1], Jeffrey Lopez [4], Daiwei Yu [7], Yanhao Dong [1✉], Weiwei Fan[1], Zhe Shi [6], Rui Xiong [1,8], Cheng-Jun Sun[9], Inhui Hwang[9], Wah-Keat Lee[5], Yang Shao-Horn [4,6,10✉], Jeremiah A. Johnson [2✉] and Ju Li [1,6✉]

By increasing the charging voltage, a cell specific energy of >400 W h kg$^{-1}$ is achievable with LiNi$_{0.8}$Mn$_{0.1}$Co$_{0.1}$O$_2$ in Li metal batteries. However, stable cycling of high-nickel cathodes at ultra-high voltages is extremely challenging. Here we report that a rationally designed sulfonamide-based electrolyte enables stable cycling of commercial LiNi$_{0.8}$Co$_{0.1}$Mn$_{0.1}$O$_2$ with a cut-off voltage up to 4.7 V in Li metal batteries. In contrast to commercial carbonate electrolytes, the electrolyte not only suppresses side reactions, stress-corrosion cracking, transition-metal dissolution and impedance growth on the cathode side, but also enables highly reversible Li metal stripping and plating leading to a compact morphology and low pulverization. Our lithium-metal battery delivers a specific capacity >230 mA h g$^{-1}$ and an average Coulombic efficiency >99.65% over 100 cycles. Even under harsh testing conditions, the 4.7 V lithium-metal battery can retain >88% capacity for 90 cycles, advancing practical lithium-metal batteries.

There is an urgent demand for high-energy-density batteries[1,2] for portable electronic devices, drones and electric vehicles. While state-of-the-art lithium-ion batteries with graphite anodes have a cell-level[3,4] gravimetric energy density ($E_g$) of ~250 W h kg$^{-1}$, a much higher $E_g$ of >400 W h kg$^{-1}$ is in principle possible for lithium-metal batteries (LMBs) with high-energy-density cathodes such as nickel-rich LiNi$_x$Mn$_y$Co$_{1-x-y}$O$_2$ (NMC)[5,6] and lithium metal anodes (LMAs). Achieving this goal requires great efforts in battery design and optimization, with elevated charging voltage and minimized excess components[3,7,8] (for example, LMAs and electrolyte), pushing all materials and cell parameters to their limits.

On the cathode side, elevating the upper cut-off voltage[1] is a straightforward way to increase the discharge capacity and energy density[9]. For example, an additional ~15–35% capacity could be gained by increasing the upper cut-off voltage of NMC cathodes from the traditional 4.3 V to 4.7 V (versus Li$^+$/Li)[10]. Unfortunately, this approach tends to induce instabilities in the bulk and at the surface of the cathode and thus significantly degrades cycle life. Such degradations become more serious[6,11] with increasing Ni content and higher cut-off voltage, especially for LiNi$_{0.8}$Co$_{0.1}$Mn$_{0.1}$O$_2$ (NMC811) of commercial interest. On the anode side, high reversibility[12,13] is essential to reduce the usage of excess lithium metal and electrolyte relative to the cathode. Finally, LMBs need to operate under practical conditions where a high-loading cathode (typical industry level is >3.5 mA h cm$^{-2}$), low negative to positive (N/P)

ratio[13] and lean electrolyte (typical industry level for electrolyte to capacity (E/C) ratio is ~2–5 g (Ah)$^{-1}$) are required at the same time. These harsh conditions make it extremely difficult to maintain a satisfactory cycle life.

Many cathode degradation mechanisms are intensified in LMBs operated under high cut-off voltages (Fig. 1a,b), including cathode–electrolyte side reactions[14–16], bulk and surface phase transformation[17], cracking of the NMC secondary particles[17,18], over-growth of cathode–electrolyte interphases (CEIs), gas evolution[15] and transition metal (TM) dissolution[19]. Moreover, dissolved TMs eventually waft to the anode side where they can be reduced and accumulated, similar to the 'shuttling effect'[20,21] in lithium–sulfur batteries, leading to the destruction of the anode's solid–electrolyte interphase (SEI), consumption of active Li, and impedance growth. Also, failures[3,7,8] often occur on the LMA as the electrolyte influences the cycling morphology and reversibility of the LMA[22]. A limited cyclable Li inventory can be easily depleted by side reactions or become kinetically unreachable due to electronic/ionic isolation[23]. Lean electrolyte itself can also be rapidly depleted or contaminated by side reactions[24], and loss of ionic percolation can happen due to wetting of large-surface-area and large-thickness Li deposits.

Since the aforementioned challenges in high-voltage LMBs are closely related to the electrolyte, the design of novel liquid electrolytes, which have the desired compatibility with both high-voltage cathodes and LMAs, offers a promising solution.
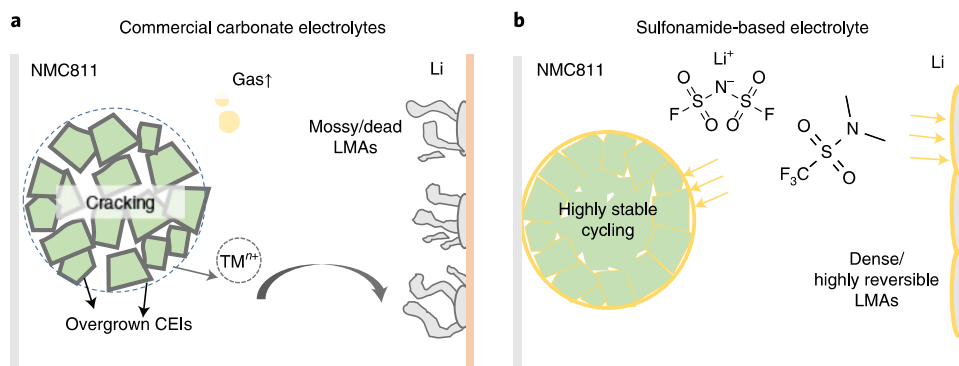
**Fig. 1 | Challenges for durable high-voltage Li‖NMC811 cells. a**, With commercial carbonate electrolytes, severe side reactions between reactive NMC811 surfaces and electrolytes lead to serious gas evolution, TM dissolution, particle cracking and overgrown CEIs. Challenges in the LMA come from the formation of mossy/dead Li, severe side reactions and TM shuttling from the cathode side. **b**, Our sulfonamide-based electrolyte can suppress/delay particle cracking and mitigate cathode–electrolyte interfacial reactions, thus enabling a highly stable cathode. Our electrolyte also favours the formation of compact uniform Li and suppresses detrimental side reactions, thus enabling a highly reversible LMA.

High-concentration electrolytes[16,25,26], localized high-concentration electrolytes[8,27], 'full-fluorine electrolytes'[28,29], fluorinated ether-based electrolytes[30,31] and cyclic phosphate-based electrolytes[32] also show promise to enhance the cycling stability of Li‖NMC batteries, yet the upper cut-off voltage reported to date is mostly limited to 4.5 V versus Li+/Li. Moreover, it should be emphasized that the claimed improvements should be carefully evaluated under practical harsh conditions[7,8].

In the present work, we demonstrate a liquid electrolyte that enables stable ultra-high-voltage cycling (~4.7 V) of a high-nickel cathode (commercial NMC811) in practical LMBs (summary of prior work in Supplementary Table 1). In order to achieve compatibility with both high-voltage NMC811 and lithium metal, we selected the liquid aprotic *N,N*-dimethyltrifluoromethane-sulfonamide (DMTMSA) as the electrolyte solvent[33,34], which belongs to the sulfonamide family. A regular concentration (1 m, where m stands for molality) of LiFSI with DMTMSA (referred to as 1 m LiFSI/DMTMSA hereafter) enables highly reversible LMAs by favouring compact Li metal deposition morphologies and minimizing pulverization. It also enables stable cycling of NMC811 cathodes under 4.7 V with a high specific capacity of >230 mA h g⁻¹ and an average Coulombic efficiency (CE) of >99.65% over 100 cycles, by suppressing cathode particle intergranular stress corrosion cracking (SCC), partially due to decreased TM ion solubility in the sulfonamide-based electrolyte. Together with cathode optimizations[35,36], this work points towards achieving durable ultra-high-voltage Ni-rich cathodes in practical LMBs.

## The 1 m LiFSI/DMTMSA enables stable cycling of 4.7 V NMC811

Our 1 m LiFSI/DMTMSA electrolyte shows good Li+ conductivity (Supplementary Table 2), good oxidation stability, compatibilities with high-voltage cathodes and the LMA and other benefits including good resistance to residual water and good wettability with separator (Supplementary Fig. 1 and Table 3). The cycling stability of 4.7 V NMC811 was tested with our 1 m LiFSI/DMTMSA electrolyte. A commercial carbonate electrolyte—1 M lithium hexafluorophosphate in ethylene carbonate and ethyl methyl carbonate (3:7 by weight) with 2 wt% vinylene carbonate (abbreviated as 1 M LiPF₆/EC-EMC + 2% VC hereafter, where M stands for molarity)—was used as the reference electrolyte.

To exclude the effect from LMA and investigate the 'intrinsic' cathode performance (Supplementary Fig. 2), a 'super-excessive condition' (thick Li metal, ~350 µm, and abundant electrolyte, ~80 µl)

was used with the reference electrolyte (blue curves in Fig. 2a), which showed 76.1% capacity retention after 100 cycles at 0.5 C and low CEs of ~98% at the end of the cycling. In contrast, our 1 m LiFSI/DMTMSA electrolyte delivered a high discharge capacity of 231 mA h g⁻¹ at 0.1 C, superior capacity retention of 88.1% after 100 cycles at 0.5 C and a high average CE of >99.65% (red curves in Fig. 2a) even under a 'stringent condition' (thin Li foil, ~60 µm, and limited electrolyte, ~20 µl), for which the reference electrolyte failed rapidly (Supplementary Fig. 2a). Despite the harsher testing conditions, our electrolyte showed less voltage decay (Fig. 2b), higher energy efficiency (Fig. 2c), higher first-cycle CE (Supplementary Fig. 3a) and more-stable voltage profiles (Fig. 2e) compared to the reference electrolyte (Fig. 2a–d and Supplementary Fig. 3b). An impressive average energy efficiency of ~97% (over 100 cycles)—a key factor for battery charging cost[37]—can also be achieved in 4.7 V NMC811, readily surpassing the target energy efficiency of 90–95% for next-generation high-voltage NMC[1].

Our electrolyte also improves rate capability (Supplementary Fig. 3c), offering high capacities of 205 mA h g⁻¹ at 1 C and 186 mA h g⁻¹ at 2 C. Moreover, the 4.7 V LMBs with our electrolyte exhibit excellent CEs of >99% even when cycled at 55 °C, compared to CEs of ~92% for the reference electrolyte (Supplementary Fig. 4). Considering the high-voltage instability of VC[38], the Li‖NMC811 cell with 1 M LiPF₆/EC-EMC without VC was tested, which showed more capacity loss upon cycling at 25 °C (Supplementary Fig. 5) than the one with VC. Nevertheless, the cycling performance of both carbonate electrolytes is far worse than that of our 1 m LiFSI/DMTMSA electrolyte. Lastly, the superior cycling performance of our electrolyte is again demonstrated when cycled with lower cut-off voltages of 4.3 V and 4.5 V (Supplementary Fig. 6).

To gain insights into the degradation mechanisms, we conducted galvanostatic intermittent titration technique measurements for the cells after the 1st and 100th cycles. It is noted that the overpotentials of the cathode cycled in our electrolyte were much smaller than the one cycled in the reference electrolyte (Fig. 2f). Moreover, we note that the open-circuit voltage profiles (dashed curves in Supplementary Fig. 7a,b; consisted of data points after each relaxation step) barely change for all the samples, which suggests that the degradation of 4.7 V NMC811 under these conditions has a kinetic origin, guiding us to carefully inspect side reactions at the cathode surface (forming a high-impedance surface phase and CEIs) as well as inside the secondary particles. Lastly, before turning to detailed analysis of the NMC cathode and LMA, we emphasize that Al corrosion is suppressed in our electrolyte (LiFSI is known to corrode an
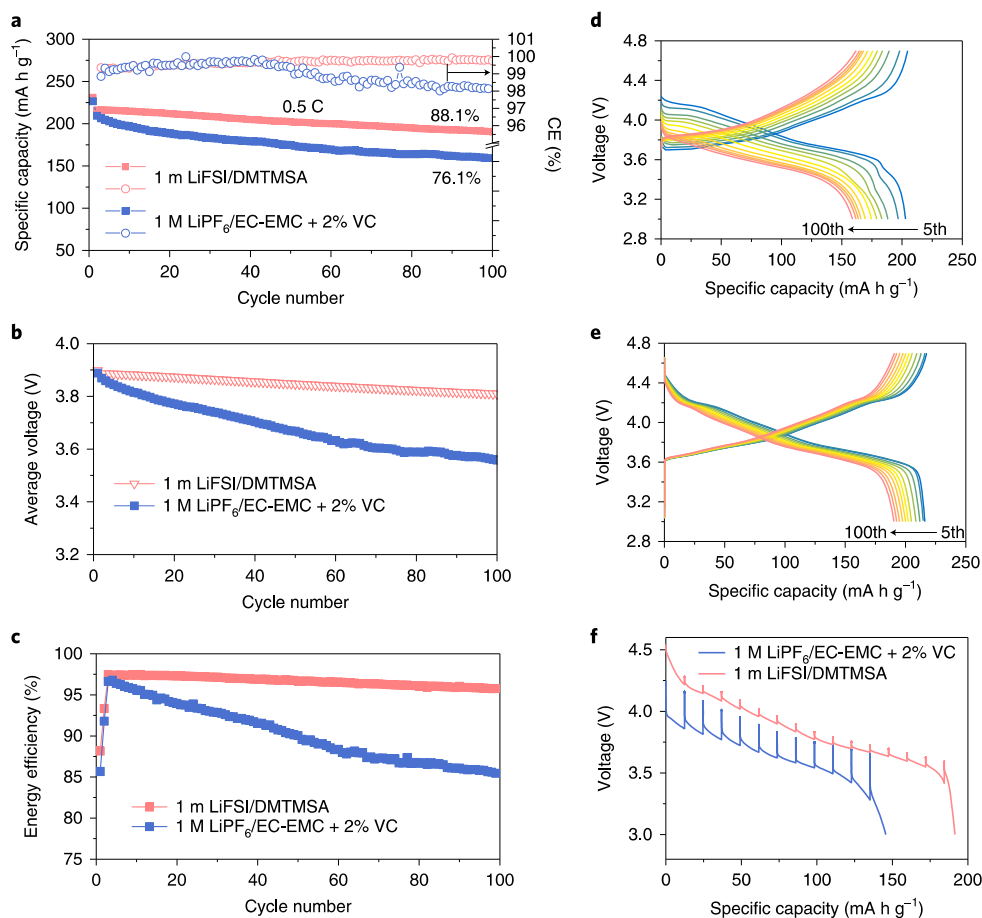
**Fig. 2 | Electrochemical performances of Li‖NMC811 cells using different electrolytes. a–c**, Specific capacity and CE (**a**), average voltage (**b**) and energy efficiency (**c**) of the investigated electrolytes at 0.5 C (0.1 C for the first cycle). **d**,**e**, Corresponding voltage profiles of the cells using 1M LiPF$_6$/ EC-EMC + 2% VC (**d**) and 1m LiFSI/DMTMSA (**e**) electrolytes. The curves in rainbow colours correspond to the voltage profiles from the 5th to 100th cycles. **f**, Discharge voltage profiles of galvanostatic intermittent titration technique measurements on the cells after 100 cycles. For cells with 1m LiFSI/ DMTMSA electrolyte, 'stringent conditions' (60 μm Li foil and 20 μl electrolyte) were used. For cells with 1M LiPF$_6$/EC-EMC + 2% VC electrolyte, 'super-excessive conditions' (350 μm Li foil and 80 μl electrolyte) were used.

Al current collector, which limits its practical use) via the formation of an AlO$_x$F$_y$-like passivation layer (Supplementary Fig. 8) similar to that formed in LiPF$_6$-based electrolyte, which does not have the Al corrosion problem[39].

### The 1m LiFSI/DMTMSA suppresses cathode–electrolyte side reactions

To evaluate the side reactions between the NMC811 cathode and the electrolyte, we conducted accelerated degradation tests by continuously exposing the cathode to the most extreme electrochemical conditions at 4.7 V versus Li⁺/Li. The 4.7 V float-test leakage current (Fig. 3a), which characterizes the side reaction rates, suggested that more side reactions happened for the cell cycled in the reference electrolyte than that cycled in our electrolyte (also confirmed by cathode surface morphologies in Supplementary Fig. 9). Compared to the reference electrolyte with a quasi-steady-state leakage current of ~17 μA, in ~5 h after an initial decay, the leakage current for our electrolyte monotonically decreased, reaching a minimum value of 3.2 μA at the end of a 20 h hold. This observation indicates a diminishing reaction rate and successfully passivated cathode surface.

The suppressed side reactions are further supported by much less CO$_2$ evolution (>~4.3 V) in our electrolyte (Fig. 3c) than in the reference one (Fig. 3d), measured by in situ differential

electrochemical mass spectrometry (DEMS), without invoking other gas production (O$_2$, SO$_2$ and NO$_2$; Fig. 3c,d and Supplementary Fig. 10) up to 4.7 V versus Li⁺/Li. Meanwhile, simultaneously suppressed TM dissolution is confirmed by inductively coupled plasma mass spectrometry (ICP-MS) measurements in Fig. 3b: after 100 cycles, an eightfold decrease in dissolved Ni and fourfold decrease in total TMs were achieved in our electrolyte with respect to the reference electrolyte.

To further characterize CEIs, X-ray photoelectron spectroscopy (XPS) measurements were conducted on the surface of the cathodes after the 100 cycles. Compared to the cathode cycled in the reference electrolyte (Fig. 3e,g), the one cycled in our electrolyte has a weaker C 1s signal (Fig. 3f, especially the peaks that can be attributed to C−O, C=O and poly(CO$_3$)) and stronger F 1s signal (Fig. 3h, especially the peak that can be attributed to F−Li). They indicate that the CEIs derived from our electrolyte should consist of more LiF-like inorganic components (which are known to be 'good' CEI components[12,26,29,30]) and less organic components (Supplementary Fig. 11). The XPS results also agree well with the time-of-flight secondary ion mass spectrometry (TOF-SIMS) measurements (Supplementary Fig. 12), where more LiF$_2^-$ (representing inorganic components) and less C$_2$HO$^-$ (representing organic components) fragments are detected for the cathode cycled with our electrolyte that the one with the reference electrolyte.
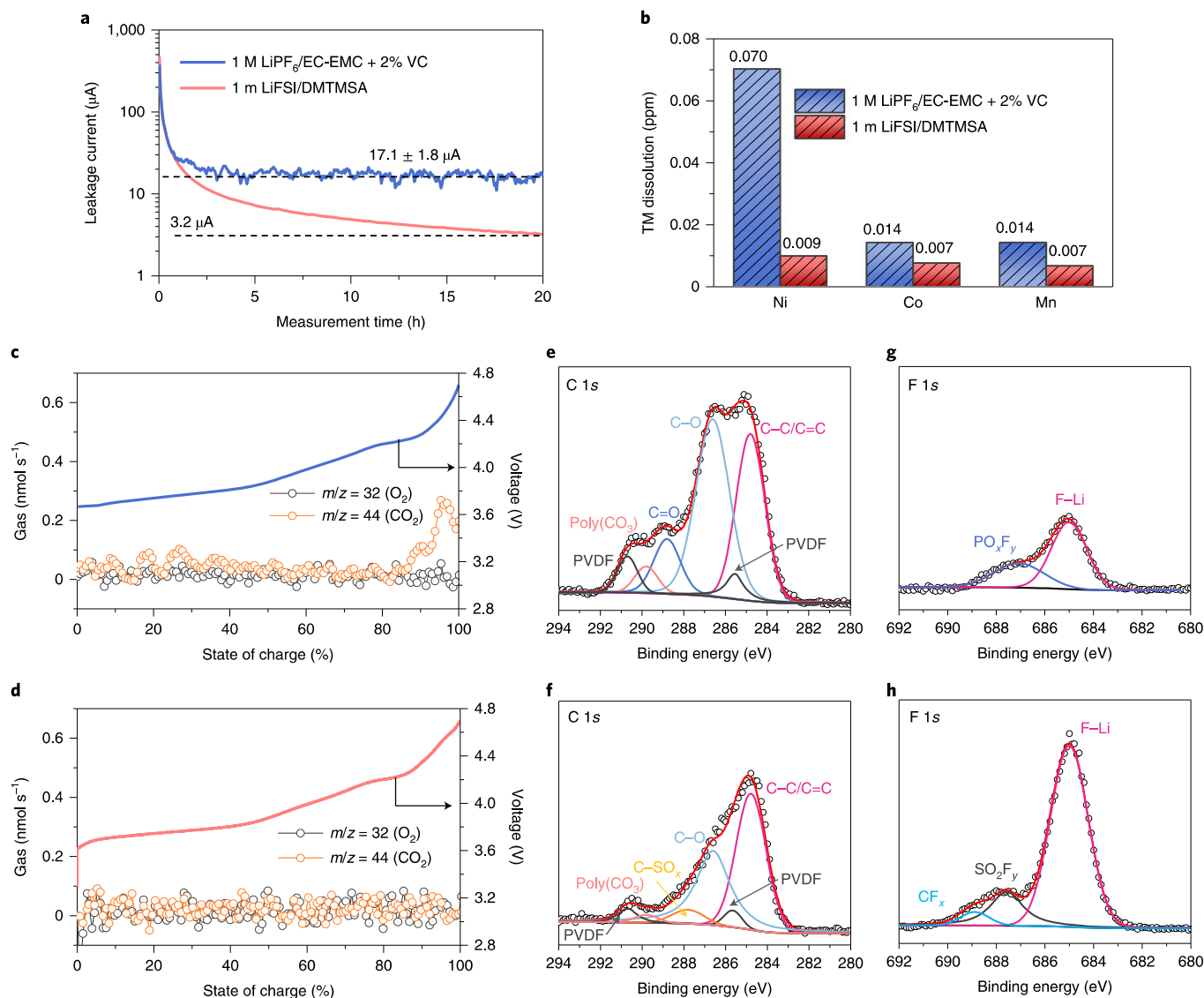
**Fig. 3 | Characterizations of cathode–electrolyte side reactions and CEIs at 4.7 V cut-off voltage. a**, Leakage currents during 4.7 V constant-voltage floating test of the NMC811 cathodes cycled in different electrolytes for 50 cycles. **b**, TM dissolution measured by ICP-MS after 100 cycles in different electrolytes. **c,d**, In situ DEMS analysis in half cells to monitor the gas evolution during first charging in 1 M LiPF$_6$/EC-EMC + 2% VC (**c**) and 1 m LiFSI/ DMTMSA (**d**) electrolytes. Voltages profiles during charging are plotted as right y axis. **e–h**, XPS analysis for the NMC811 cathodes cycled in 1 M LiPF$_6$/ EC-EMC + 2% VC (**e** and **f**) and 1 m LiFSI/DMTMSA (**g** and **h**) electrolytes for 100 cycles. PVDF, polyvinylidene fluoride. The black dots and red lines are original and fitted XPS spectra, respectively. The devolution spectra in different colours correspond to the labelled chemistries near the spectra.

## The 1 m LiFSI/DMTMSA suppresses microstructural degradation

Intergranular cracking between connected primary particles in a secondary particle is a critical issue for the degradation of Ni-rich cathodes, especially with higher cut-off voltages and prolonged cycling[40,41], resulting in the loss of electrical contacts between primary particles. An increased electrochemical surface area also means more liquid electrolyte required for wetting (the liquid electrolyte in industry batteries, ~2–5 g A$^{-1}$ h$^{-1}$, needs to wet the cathode, anode and separator, often making it the scarcest component), more side reactions and more electrolyte consumption. This phenomenon is apparently severe for the NMC811 cathodes cycled in the reference electrolyte, as the galvanostatic intermittent titration technique after cycling identified large overpotential growth in the form of ohmic loss (Supplementary Fig. 7) that is closely related to electron transport at the electrode level.

To characterize such microstructural degradation, cathodes after 100 cycles were cross-sectioned and inspected under scanning electron microscopy (SEM). While extensive cracking can be observed in the cathode cycled with the reference electrolyte (Fig. 4a,b), it is apparently suppressed or delayed with our electrolyte (Fig. 4c,d). More examples can be found in Supplementary Fig. 13. Note that complete elimination of the cracking is still challenging if ever possible, but it may not be a necessary condition to achieve a satisfactory cycling performance over a hundred cycles.) The morphology of cycled NMC811 secondary particles was next examined by three-dimensional tomography of the full-field X-ray imaging (FXI) at the National Synchrotron Light Source II (Brookhaven National Laboratory). The reconstructed images clearly contrast the cracking behaviour with the reference electrolyte (Fig. 4e, with severe cracking along radial direction) and our electrolyte (Fig. 4f, with intact primary particles).
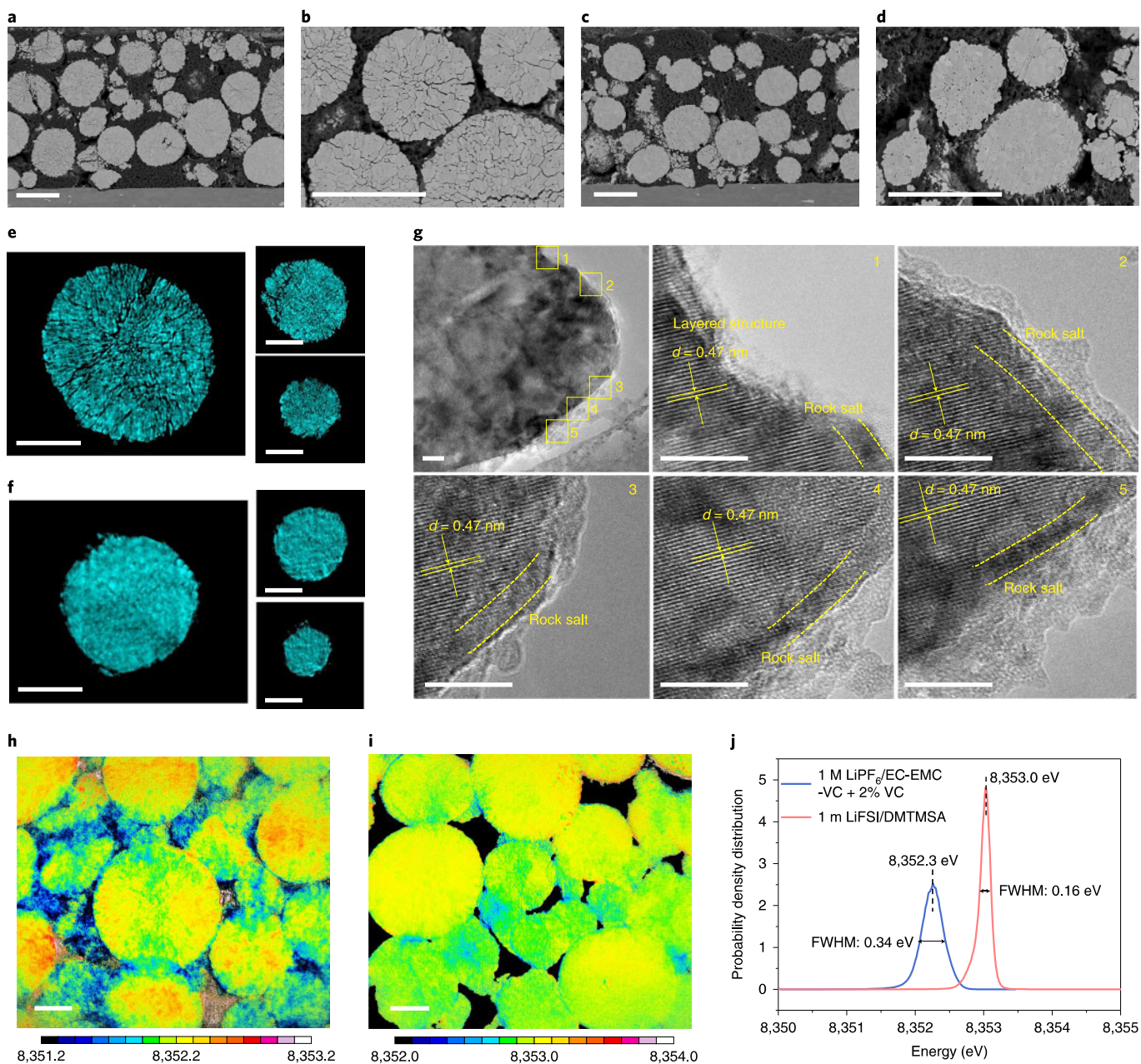
**Fig. 4 | Structural characterizations of the cycled NMC811 cathodes with different electrolytes. a–d**, SEM images of cross-sectioned NMC811 cathodes cycled in 1 M LiPF$_6$/EC-EMC + 2% VC (**a** and **b**) and 1 m LiFSI/DMTMSA (**c** and **d**) electrolytes. **e,f**, Two-dimensional cross-sections at different depths of the reconstructed three-dimensional tomography images of NMC particles cycled in 1 M LiPF$_6$/EC-EMC + 2% VC (**e**) and 1 m LiFSI/DMTMSA (**f**) electrolytes. **g**, High-resolution TEM images of NMC811 particles cycled in 1 m LiFSI/DMTMSA electrolyte. *d*, distance between lattice planes. **h,i**, Two-dimensional XANES mapping of NMC811 particles cycled in 1 M LiPF$_6$/EC-EMC + 2% VC (**h**) and 1 m LiFSI/DMTMSA (**i**) electrolytes for 100 cycles and then charged to 4.7 V versus Li$^+$/Li. The colour bars correspond to the white line peak position in eV. **j**, Statistical analysis of the whiteline distributions in particles in **h** and **i**. A smaller full width at half maximum (FWHM) in **j** represents less-scattered Ni oxidation states. Scale bars, 10 μm (**a–d**), 5 μm (**e,f,h,i**) and 10 nm (**g**).

The surface phase transition from a layered to resistive rock-salt NiO-like structure is known to degrade NMC cathode performance. Under high-resolution transmission electron microscopy (TEM), we found the transformed rack-salt layer is thin (~3–4 nm) and uniform (shown by panels 1–5 of Fig. 4g, taken from five local regions) over the surface of the cathode cycled in our electrolyte, while the one cycled with the reference electrolyte has a very thick rock-salt layer of >20 nm (Supplementary Fig. 14). This finding agrees well with the improved electrochemical performance by our

electrolyte, especially the suppressed impedance growth in Fig. 2g. Since oxygen loss and cation densification are obviously involved in the layered-to-rock-salt surface phase transition, it is also consistent with the suppressed side reactions presented in Fig. 3.

The redox chemistry in bulk would be significantly affected by the loss of electrical contacts and phase transitions at cracking-exposed fresh surfaces. Using the X-ray absorption near-edge structure (XANES) mode of FXI, we mapped Ni oxidation states in the cycled cathodes at the fully charged state (that is, 4.7 V versus Li$^+$/Li). We
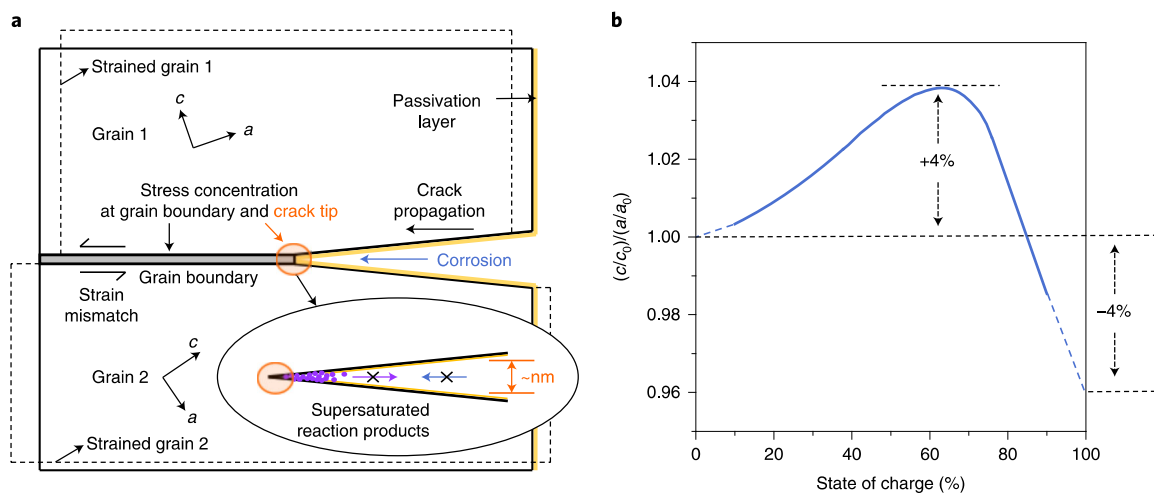
**Fig. 5 | Proposed stress-corrosion cracking (SCC) mechanism for polycrystalline cathodes and its suppression by limiting reaction-product solubilities in the liquid electrolyte. a**, Intergranular cracking beyond a purely mechanical event involves chemical interactions between the cathode grain boundary/ surface region and electrolyte. SCC can be largely suppressed by our electrolyte, because it is less reactive and corrosive and the supersaturated side reaction products cannot diffuse away in the nano-channel near the crack tip. The dashed lines are schematics of the strained grains. **b**, The lattice anisotropy $(c/c_0)/(a/a_0)$ ratio as a function of state of charge in the NMC811 cathode[47]. The dashed lines are extrapolated data to fully charged and discharged states.

found that Ni has higher and more narrowly distributed oxidation states in the sample cycled in our electrolyte (Fig. 4h) than in the reference electrolyte (Fig. 4i). Here, the whiteline analysis was conducted on the signals collected from the particles that are not overlapping with each other (Supplementary Fig. 15). Therefore, the microstructural degradation, surface phase transition and bulk electrochemistry are apparently correlated, and all three issues have been successfully addressed by our electrolyte.

Previously, intergranular cracking was mostly attributed to mechanical stress created by anisotropic lattice expansion/shrinkage and heterogeneous charge/discharge kinetics during electrochemical cycling. However, in our work, cathodes with the same composition, microstructure, electrochemistry and testing conditions (except for the amount of electrolyte and LMA) showed large differences, and intergranular cracking can be suppressed with electrolytes even under deep-charge cycling at 4.7 V (electrolyte-modified cracking behaviour was also noted in the literature[42], albeit at lower cut-off voltages). In the literature, infused cathode coating[43,44] was also reported to relieve intergranular cracking in Ni-rich cathodes, which was explained by blocking the penetration of the electrolytes. This argument does not apply to our case, since we used the same NMC811 cathode. Therefore, our observation—a 'good' electrolyte can mitigate or slow down microstructure degradation of a deep-cycled Ni-rich cathode—demonstrates that the intergranular cracking should be more than a purely stress-driven event and the chemical interaction between the charged cathode grain boundary/ surface region and electrolyte is also key. This is by definition a SCC process (Fig. 5a).

The proposed SCC mechanism is consistent with the observation that single-crystalline NMC (and LiCoO$_2$) with a similar size as the secondary particles of polycrystalline NMC does not crack as easily[45,46], indicating that uniform eigenstrain (that is, stress-free strain induced by lithiation/delithiation chemical expansion) does not crack the brittle ceramic particles despite its relatively large magnitude. It is the large linear-strain mismatch at grain boundaries[47]—given the ±4% change in anisotropic ratio $(c/c_0)/(a/a_0)$ during charge/discharge (Fig. 5b); here $a_0$ and $c_0$ denote the lattice parameters in fully discharged state, and $a$ and $c$ denote the lattice parameters during charge/discharge—that leads to either large elastic stress (~6 GPa with ~140 GPa Young's modulus[48]) or slippage

(inelastic grain boundary sliding). Note the 6 GPa elastic stress does not even account for the concentration factor at the potential mode-II, mode-III or mixed-mode crack tip at grain boundary. The suppressed/delayed mode-I cracking in a 'good' electrolyte indicates that inelastic grain boundary slippage could relax stress build-up and cleavage. On the other hand, a 'bad' electrolyte can worsen the situation, where continuous side reactions corrode the cyclically slipping grain boundaries. Oxygen loss and TM dissolution into the electrolyte offer thermodynamic and kinetic advantage to the initiation and propagation of SCC and degrade the cathodes. The hypothetical SCC mechanism and its mitigation provide new insights into the intertwined electro-chemo-mechanics of oxide cathodes under extreme electrochemical conditions and synergize with recent progress in optimizing bulk electrode composition and crystallography[35,36].

## Improved Li metal reversibility

Beyond the cathode, the cycling stability of LMBs also heavily relies on the compatibility between the electrolyte and LMA. Figure 6a shows the CEs evaluated by Li stripping/plating on Cu current collectors, where our 1 m LiFSI/DMTMSA electrolyte has an average CE of ~99% over 345 cycles, much higher than that of the reference electrolyte. The superior compatibility of our electrolyte was further demonstrated by the stable cycling of Li∥Li symmetric cells in Fig. 6b, which shows much less polarization than the cells using the reference electrolyte. Moreover, our electrolyte enables remarkably stable cycling in an 'anode-free' cell consisting of a bare Cu current collector and high-loading NMC811 cathode with limited electrolyte (Supplementary Fig. 16). These results demonstrate excellent compatibility between our electrolyte and the LMA.

The Li metal morphology is critical to LMA reversibility. After long-term cycling, the thickness of LMA increases due to Li metal morphological instability, which contains SEIs, trapped gases[30] and liquid-infilled porosity. A less-compact, less-active layer, formed by dead Li, SEIs and high porosity, together with depleted Li inventory and liquid electrolyte (also contaminated), leads to impedance growth and premature cell failure on the anode side. It is also a safety risk in the event of accidents. This is the case for the LMA cycled in the reference electrolyte (Supplementary Fig. 17), where active Li was completely consumed, with a hugely swollen LMA
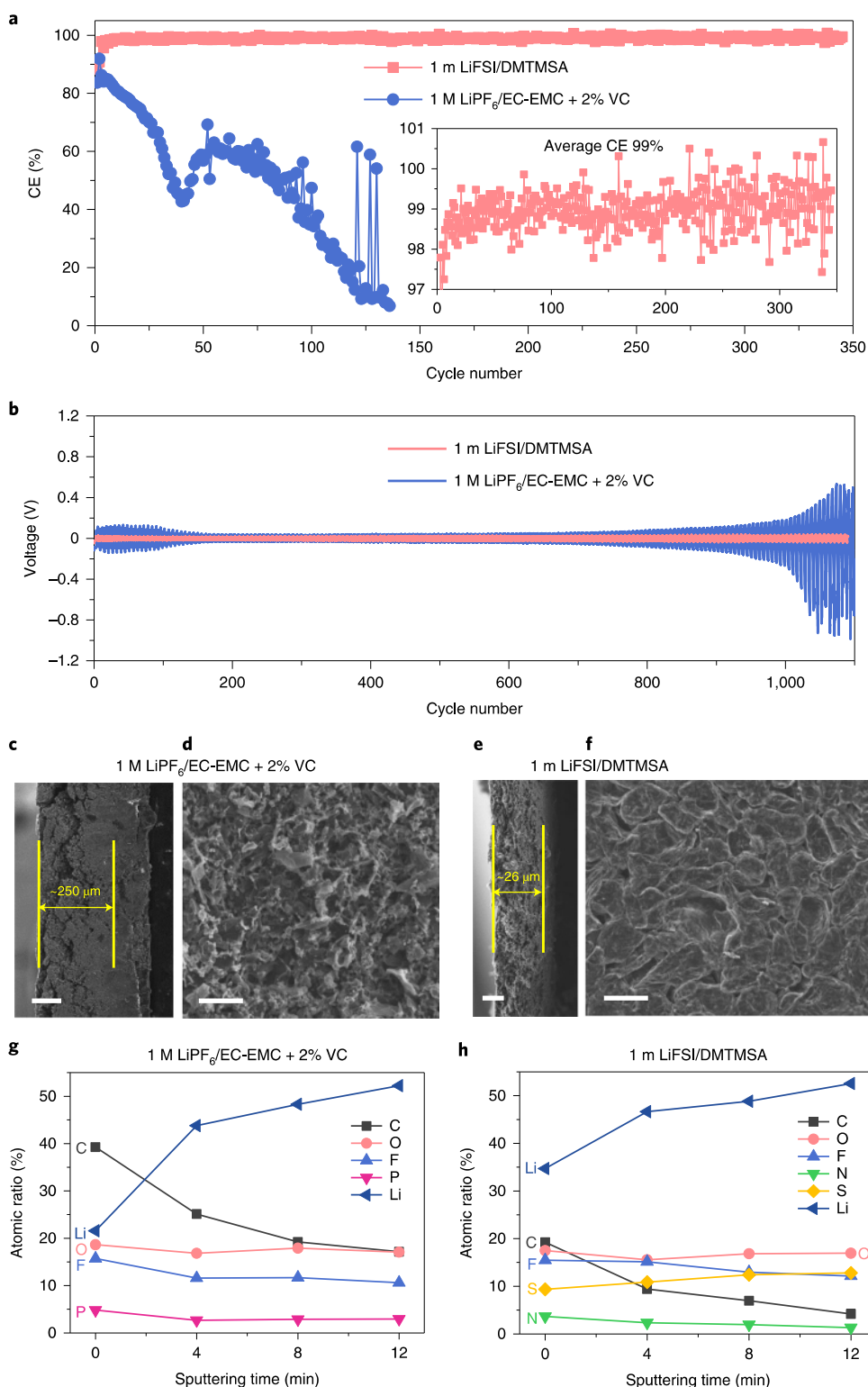
**Fig. 6 | Electrochemical performance and characterizations of the LMA in different electrolytes. a**, Li metal plating/stripping CEs evaluated by Li‖Cu coin cells at $0.5\,mA\,cm^{-2}$ and $1\,mA\,h\,cm^{-2}$. Inset is the enlarged figure of CEs. **b**, Cycling stability demonstrated by Li plating/stripping in Li‖Li symmetric cells at $0.5\,mA\,cm^{-2}$ and $1.5\,mA\,h\,cm^{-2}$. **c–f**, SEM images illustrating the cross-section views (**c** and **e**) and the surface morphology (**d** and **f**) of the LMA collected from Li‖NMC811 cells with the investigated electrolytes after 100 cycles at 0.5 C. **g**,**h**, SEI information obtained by the quantified atomic ratios of different elements by XPS conducted on the LMA after 100 cycles in $1\,M\,LiPF_6/EC\text{-}EMC + 2\%$ VC (**g**) and $1\,m$ LiFSI/DMTMSA (**h**) electrolytes. Scale bars, $100\,\mu m$ (**c**), $5\,\mu m$ (**d** and **f**) and $10\,\mu m$ (**e**).

from an initial thickness of $60\,\mu m$ to $\sim\!250\,\mu m$ (Fig. 6c). By contrast, the thickness increase was an order of magnitude less, and the less-compact layer was only $\sim\!26\,\mu m$ thick (Fig. 6e), after cycling in

our electrolyte. The Li particles remain larger, uniform and compact (Fig. 6f), while whisker-like Li deposits with high porosity can be observed in the case of the reference electrolyte (Fig. 6d).
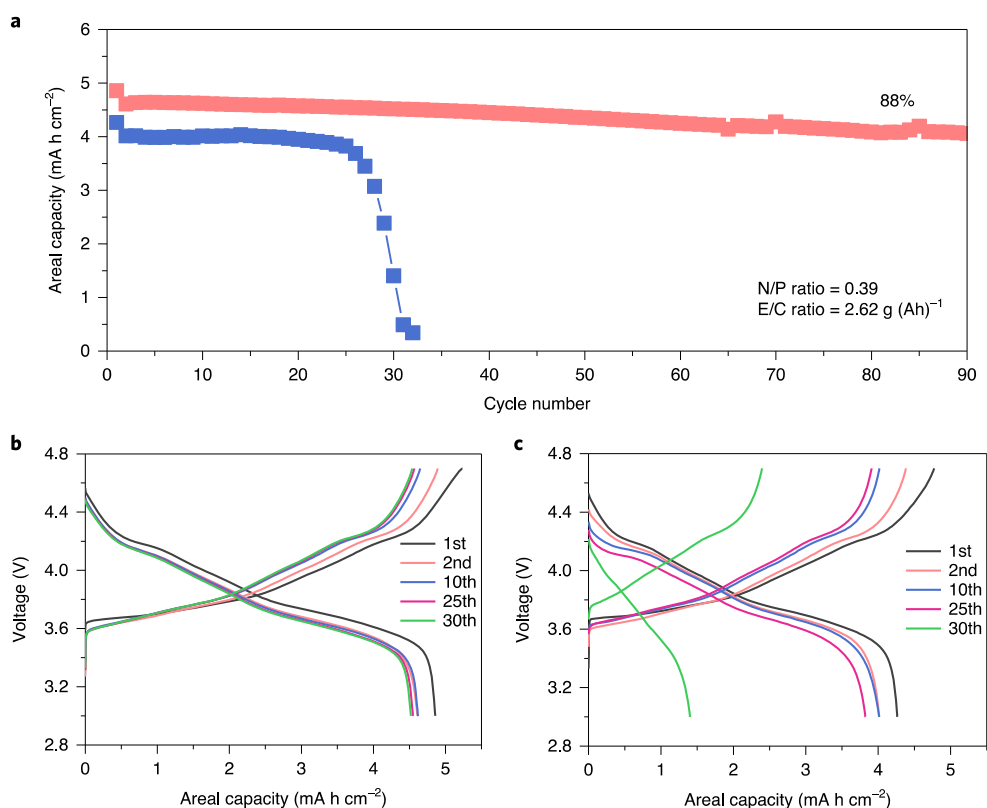
**Fig. 7 | Electrochemical performance of Li‖NMC811 cells under practical conditions. a–c**, Cycling performance (**a**) and corresponding voltage profiles of the coin cells with high-loading NMC811 cathodes (>4 mA h cm$^{-2}$) at 4.7 V cut-off voltage using 1 m LiFSI/DMTMSA (**b**) and 1 M LiPF$_6$/EC-EMC + 2% VC (**c**) electrolytes. The discharging/charging rates were 0.1 C/0.1 C for the first cycle and 0.5 C/0.15 C afterwards. For 1 m LiFSI/DMTMSA electrolyte, the N/P and E/C ratios were ~0.39 and ~2.62 (g (Ah)$^{-1}$). For 1 M LiPF$_6$/EC-EMC + 2% VC electrolyte, the N/P ratio was ~2.8 (60 μm Li foil was used) and the E/C ratio was ~5 g (Ah)$^{-1}$.

Moreover, different SEI compositions formed in the different electrolytes were also identified by XPS on the cycled LMA (Fig. 6g,h). It is apparent that the SEI derived from the sulfonamide-based electrolyte was mainly composed of inorganic components including LiF and lower-valence sulfur (S$^-$/S$^{2-}$) species, which are preferable SEI components[12], while that derived from the carbonate reference electrolyte was abundant with organic components (Supplementary Fig. 18). Compared to the C−C and C−O/C=O groups in carbonates, the sulfonamide group (CF$_3$SO$_2$N−) facilitates the donation of F and S to the highly reductive Li to form more favourable SEIs.

## Full-cell performance under practical conditions

To maximize the full-cell $E_g$ for LMBs, high-loading cathode, lean electrolyte and a low amount of LMA should be used simultaneously[3], which is a great challenge. When using the reference electrolyte, 4.7 V LMBs with a high-loading NMC811 cathode (~4.25 mA h cm$^{-2}$), thin Li foil (60 μm; N/P ratio ~2.82) and limited electrolyte (E/C ratio ~5 g (Ah)$^{-1}$) can survive only 25 cycles (Fig. 7a), where uncontrolled side reactions rapidly deplete the Li and/or electrolyte and cause catastrophic capacity decay (Fig. 7c). Remarkably, even under much harsher conditions (cathode loading of ~4.86 mA h cm$^{-2}$, N/P ratio of ~0.39, E/C ratio of ~2.62 g (Ah)$^{-1}$), our 1 m LiFSI/DMTMSA electrolyte enables 4.7 V LMBs with greatly improved cycling stability, achieving 88% capacity retention after 90 cycles at a 0.5 C/0.15 C discharge/charge rate (Fig. 7a,b and Supplementary Fig. 19).

Higher-rate cycling data are available in Supplementary Fig. 20, where ~0.3 C charging offers good cycling performance with

a cathode loading of ~3.5 mA h cm$^{-2}$, N/P ratio of ~1, E/C ratio of ~3.0 g (Ah)$^{-1}$ and ~0.5 C charging. To validate the achievable energy density, single-layer pouch cells were assembled and tested with different electrolytes with a cathode loading of ~18.4 mg cm$^{-2}$, E/C ratio of ~2.3 g (Ah)$^{-1}$ and N/P ratio of ~2.9 between 3.0 V and 4.7 V (Supplementary Fig. 21). The pouch cell with our electrolyte can stably deliver a specific energy of 353 W h kg$^{-1}$ (Supplementary Table 4), while the one with the reference electrolyte rapidly degrades within 20 cycles. Adapting the parameters of demonstrated multilayer pouch cells[3], we estimate a cell-level specific energy of 417 W h kg$^{-1}$ (Supplementary Table 5), which is encouraging for future development and large-scale production, and which reduces the cost (the present material costs are listed in Supplementary Table 6) of our sulfonamide electrolyte for practical high-voltage Li‖NMC811 batteries.

## Discussion

In the above, we presented the greatly improved electrochemical performance offered by our 1 m LiFSI in DMTMSA electrolyte and proved that it successfully modified cathode–electrolyte and anode–electrolyte interactions with suppressed side reactions. These findings lead to the interesting question of what the electrolyte does at the atomic level. On the anode side, weakly solvating electrolyte has been proposed[31,49] to weaken Li$^+$–solvent interactions while promoting Li$^+$–anion interactions. This creates more anion-derived SEIs, which are believed to benefit graphite[49] and LMA[31]. Our solvent DMTMSA has a weak solvation ability for salts[34] because of its low polarity[33], which together with the benefits of LiFSI makes

our 1 m LiFSI/DMTMSA electrolyte highly compatible with LMA. Meanwhile, our electrolyte has lower solubility of salts in general (compared to a carbonate electrolyte with higher polarity), including $Ni(TFSI)_2$, $Co(TFSI)_2$ and $Mn(TFSI)_2$, which have a TFSI group that is similar to that of the DMTMSA solvent (Supplementary Fig. 22). Such lowered solubilities are also expected for $Ni^{2+}/Co^{2+}/Mn^{2+}$ salts with other anion groups.

This lowered solubility could also explain the suppressed Al corrosion in the present study, because if the side reaction products between Al and LiFSI cannot be dissolved and diffuse away, they can become supersaturated and form an all-covering passivation layer (for example, the $AlO_xF_y$-like surface layer detected by XPS in Supplementary Fig. 8). And we note two additional advantages for our electrolyte compared to the carbonate ones. On one hand, EC is easy to dehydrogenate on highly delithiated NMC surfaces to form protic species, which could further react with $LiPF_6$ to generate corrosive HF[50]. By contrast, DMTMSA can avoid this issue due to its aprotic nature and good oxidation stability. On the other hand, LiFSI is more resistant to hydrolysis than $LiPF_6$ is (Supplementary Fig. 1d). All these effects should contribute to suppressed side reactions and better passivation.

Moreover, considering the SCC mechanism, the chemical corrosion attack is intensified by slippage and residual stress at grain boundaries, especially at the intergranular crack tip (Fig. 5a). It would in turn trigger faster crack propagation and catastrophic failure. However, such an issue can be largely relieved in our electrolyte, because it is less reactive (good oxidation stability) and corrosive (less HF), and the supersaturated side reaction products could not diffuse away in the nano-channel near the crack tip (Fig. 5a). It would modify the thermodynamics and kinetics of the cathode–electrolyte side reactions in a highly non-linear fashion, thus protecting the NMC811 secondary-particle architecture from intergranular SCC, driven by the cyclic grain-level anisotropic strains from lithiation/delithiation even at an extreme voltage of 4.7 V (0.94 Li removal per $LiTMO_2$).

## Conclusions

To conclude, we demonstrated a sulfonamide-based electrolyte (1 m LiFSI in DMTMSA) for LMBs paired with ultra-high-voltage NMC811 cathodes that displays superior cycling stability under harsh conditions. On the cathode side, our electrolyte can successfully enable the stable cycling of 4.7 V NMC811, delivering a specific capacity of >230 mA h g$^{-1}$ and an average CE of >99.65% over 100 cycles. Our electrolyte effectively stabilizes the NMC811 cathode surface, thus suppressing the rates of side reactions, gas evolution and TM dissolution. Detailed surface characterizations also suggest the formation of more LiF-like inorganic components inside the CEIs derived from our electrolyte compared to a commercial carbonate reference electrolyte. Moreover, the delayed intergranular SCC of NMC811 preserves electronic contacts between primary particles and prevents the need for more liquid electrolyte for wetting mode-I crack-generated fresh surfaces. On the LMA side, our electrolyte shows excellent compatibility with a desirable deposition morphology and minimized Li metal pulverization. Benefiting both electrodes of the full cell, the 1 m LiFSI/DMTMSA electrolyte enabled good cycling stability of ultra-high-voltage LMBs under industrially practical, harsh conditions. The findings of this study highlight the pivotal role of electrode–electrolyte interactions and recapitulate the tried-and-true 'electrolyte' approach for the future development of high-energy-density LMBs.

## Methods

**Materials.** NMC811 cathodes were provided by Argonne National Laboratory with an areal loading of active materials of ~7.5 mg cm$^{-2}$. NMC811 powder (with $LiB_xO_y$ coating; Supplementary Fig. 23), conductive carbon (Super C65) and 60-μm-thick Li on Cu foil were purchased from Targray, MTI and China

Energy Lithium, respectively. Commercial electrolytes—1 M $LiPF_6$ in 3:7 (by weight) EC/EMC + 2 wt% VC and 1 M $LiPF_6$ in 3:7 (by weight) EC/EMC—were purchased from Soulbrain and BASF, respectively. LiFSI salt was supplied by KISCO. $Ni(TFSI)_2$, $Co(TFSI)_2$ and $Mn(TFSI)_2$ were purchased from Sigma Aldrich. DMTMSA was synthesized following our previously reported procedure[34]. Possible residual water was removed from the salt and as-received solvent by heat treatment under vacuum and molecular sieves before use, respectively. Molality (m, moles of salt in kilograms of solvent (mol kg$^{-1}$)) and molarity (M, moles of salt in litres of solution (mol l$^{-1}$)) are used to denote the salt concentration in electrolytes. No other ingredient was employed in our sulfonamide-based electrolyte as additive.

**Characterizations.** Cycled Li and NMC811 electrodes were obtained by disassembling CR2032 coin cells in the glove box with $O_2$ and $H_2O$ level <1 ppm, and then washing them with pure dimethyl ether (DME) and dimethyl carbonate (DMC), respectively. The morphology and microstructure were obtained from high-resolution SEM (Zeiss Merlin) and TEM (JOEL 2010F). Thin-section TEM specimens were fabricated directly from the cycled NMC811 electrode by a standard lift-out procedure[43] by focused ion beam (NVision 40 CrossBeam, ZEISS). The surface chemistry of cycled electrodes was analysed by XPS (Physical Electronics Versaprobe II) and TOF-SIMS (ION-TOF). Ex situ three-dimensional tomography and transmission X-ray microscopy XANES on the cycled NMC811 electrodes sealed in Kapton film were conducted on FXI beamline at National Synchrotron Light Source II of Brookhaven National Laboratory. The bulk XANES of these samples were measured in transmission mode using 20-BM-B beamline of Advanced Photon Source at Argonne National Laboratory. Whiteline peak position tracking method[51] (Supplementary Note) was used in transmission X-ray microscopy XANES data analysis where the whiteline peak positions represent the Ni oxidation states.

In situ DEMS was used for detecting the gas evolution during cell charging at 0.03 C using different electrolytes. Details on the instrument set-up can be found elsewhere[52]. For the TM dissolution measurement, coin cells with NMC811 as the cathode and Li metal foil as the anode in different electrolytes were first assembled. Then following an established method[18], ICP-MS (Agilent 7900) was used to determine the metal concentration. Cross-sections of cycled cathodes were cut by an ion-milling machine (IM-40000, Hitachi) and inspected by SEM. The solubility of $Ni(TFSI)_2$, $Co(TFSI)_2$ and $Mn(TFSI)_2$ in both electrolytes was measured in grams per 100 g. The purity of DMTMSA was analysed with $^1$H and $^{19}$F NMR. A 3,000 ppm water was added into the 1 M $LiPF_6$/EC-EMC + 2 wt% VC and 1 m LiFSI/DMTMSA electrolytes and aged for several days. The water contents in the electrolyte before and after ageing were measured by Karl Fisher titration (Metler-Toledo). The viscosity was measured using a SVM3001 viscometer (Anton Paar).

A conductivity cell with two platinum-black electrodes was used to measure the Li ion conductivity. Standard solution (0.01 M KCl aqueous solution, 1.41 mS cm$^{-1}$) was used to calibrate the cell constant. The conductivity cell was immersed into electrolyte and the Li ion conductivity was measured by the impedance method with a frequency ranging from $10^6$ to $10^1$ Hz (Gamry Reference 600+). The transference number of Li$^+$ ($t_+$) was evaluated by the method proposed by Bruce and Vincent[53]. For evaluating the wettability of different electrolytes, the electrolyte was first dropped onto Celgard 2325 separator and then the contact angle was measured by a contact angle meter (SL200B, KINO Scientific Instrument).

**Electrochemical measurements.** CR2032 coin cells were prepared using NMC811 as the cathode, Celgard 2325 (polypropylene–polyethylene–polypropylene) as the separator and a Li metal anode in the glove box. For cathodes with high areal loading, NMC811, Super C65 and polyvinylidene fluoride binder in a weight ratio of 94:3:3 were first mixed with N-methyl-2-pyrrolidone to form a uniform slurry, which was coated onto Al foil using a doctor blade. The thickness was ~96 μm for the high-loading NMC811 cathode and ~52 μm for the low-loading NMC811 cathode, both including 15-μm-thick Al foil. The porosity was ~33% for the high-loading NMC811 cathode and ~36% for the low-loading NMC811 cathode. Then the coated electrodes were dried at 120 °C overnight. Finally, the electrodes were rolled and punched.

Li metal foils with 350 μm and 60 μm (on Cu) were used. The Li anode paired with high-loading NMC811 cathodes in the coin cell was fabricated by electrochemical deposition on Cu foil without pretreatment. Electrolyte amounts in coin cells were carefully controlled by pipette. Landt CT 2001A and BTS9000 Neware cyclers were used to perform galvanostatic cycling at different C rates (1 C is 200 mA g$^{-1}$). The galvanostatic intermittent titration technique was performed on cycled coin cells within a voltage range of ~3.0–4.7 V with current pulse intervals at ~0.5 C for 8 minutes, followed by 60-minute rests. The electrochemical floating test was performed in coin cells with NMC811 and Li metal as cathode and anode, respectively, in different electrolytes. The cells were first charged to 4.7 V at 0.1 C and then maintained for 20 h with the current monitored by the Neware cycler.

The cathodes for SEM observation after the floating test were collected by dissembling the cells and then washing with DMC three times. The electrochemical stability of electrolytes was evaluated by a linear sweep voltammetry method at a scan rate of 10 mV s$^{-1}$ using a Li∥Al configuration. The stability of the Al current collector in different electrolytes at high voltages was

measured by a Li ‖ Al configuration while holding the potential at 4.7 V for 10 h. Then the Al foils were collected and characterized by SEM and XPS. Single-layer pouch cell was assembled by hand-stacking the NMC811 cathode, Li foil (on Cu current collector) and separator, followed by electrolyte injecting and vacuum sealing. The gravimetric energy density of the jellyroll pouch cell was calculated based on the mass of cathode, anode, separator and electrolyte.

## Data availability
The datasets analysed and generated during the current study are included in the paper and its Supplementary Information.

## References
1. Li, W., Erickson, E. M. & Manthiram, A. High-nickel layered oxide cathodes for lithium-based automotive batteries. *Nat. Energy* **5**, 26–34 (2020).
2. Xue, W. et al. Intercalation-conversion hybrid cathodes enabling Li–S full-cell architectures with jointly superior gravimetric and volumetric energy densities. *Nat. Energy* **4**, 374–382 (2019).
3. Liu, J. et al. Pathways for practical high-energy long-cycling lithium metal batteries. *Nat. Energy* **4**, 180–186 (2019).
4. Xue, W. et al. Gravimetric and volumetric energy densities of lithium-sulfur batteries. *Curr. Opin. Electrochem.* **6**, 92–99 (2017).
5. Manthiram, A., Song, B. & Li, W. A perspective on nickel-rich layered oxide cathodes for lithium-ion batteries. *Energy Storage Mater.* **6**, 125–139 (2017).
6. Noh, H.-J., Youn, S., Yoon, C. S. & Sun, Y.-K. Comparison of the structural and electrochemical properties of layered $Li[Ni_xCo_yMn_z]O_2$ (x=1/3, 0.5, 0.6, 0.7, 0.8 and 0.85) cathode material for lithium-ion batteries. *J. Power Sources* **233**, 121–130 (2013).
7. Ren, X. et al. Enabling high-voltage lithium-metal batteries under practical conditions. *Joule* **3**, 1662–1676 (2019).
8. Niu, C. et al. Self-smoothing anode for achieving high-energy lithium metal batteries under realistic conditions. *Nat. Nanotechnol.* **14**, 594–601 (2019).
9. Li, W., Song, B. & Manthiram, A. High-voltage positive electrode materials for lithium-ion batteries. *Chem. Soc. Rev.* **46**, 3006–3059 (2017).
10. Ahmed, S. et al. Cost of automotive lithium-ion batteries operating at high upper cutoff voltages. *J. Power Sources* **403**, 56–65 (2018).
11. Jung, R., Metzger, M., Maglia, F., Stinner, C. & Gasteiger, H. A. Chemical versus electrochemical electrolyte oxidation on NMC111, NMC622, NMC811, LNMO, and conductive carbon. *J. Phys. Chem. Lett.* **8**, 4820–4825 (2017).
12. Xue, W. et al. FSI-inspired solvent and 'full fluorosulfonyl' electrolyte for 4 V class lithium-metal batteries. *Energy Environ. Sci.* **13**, 212–220 (2020).
13. Suo, L. et al. Fluorine-donating electrolytes enable highly reversible 5-V-class Li metal batteries. *Proc. Natl Acad. Sci. USA* **115**, 1156–1161 (2018).
14. Ma, L., Nie, M., Xia, J. & Dahn, J. R. A systematic study on the reactivity of different grades of charged $Li[Ni_xMn_yCo_z]O_2$ with electrolyte at elevated temperatures using accelerating rate calorimetry. *J. Power Sources* **327**, 145–150 (2016).
15. Jung, R., Metzger, M., Maglia, F., Stinner, C. & Gasteiger, H. A. Oxygen release and its effect on the cycling stability of $LiNi_xMn_yCo_zO_2$(NMC) cathode materials for Li-ion batteries. *J. Electrochem. Soc.* **164**, A1361–A1377 (2017).
16. Laszczynski, N., Solchenbach, S., Gasteiger, H. A. & Lucht, B. L. Understanding electrolyte decomposition of graphite/NCM811 cells at elevated operating voltage. *J. Electrochem. Soc.* **166**, A1853–A1859 (2019).
17. Ryu, H.-H., Park, K.-J., Yoon, C. S. & Sun, Y.-K. Capacity fading of Ni-rich $Li[Ni_xCo_yMn_{1-x-y}]O_2$ (0.6 ≤ x ≤ 0.95) cathodes for high-energy-density lithium-ion batteries: bulk or surface degradation? *Chem. Mater.* **30**, 1155–1163 (2018).
18. Xu, G.-L. et al. Building ultraconformal protective layers on both secondary and primary particles of layered lithium transition metal oxide cathodes. *Nat. Energy* **4**, 484–494 (2019).
19. Li, W., Kim, U. H., Dolocan, A., Sun, Y. K. & Manthiram, A. Formation and inhibition of metallic lithium microstructures in lithium batteries driven by chemical crossover. *ACS Nano* **11**, 5853–5863 (2017).
20. Xue, W. et al. Manipulating sulfur mobility enables advanced Li-S batteries. *Matter* **1**, 1047–1060 (2019).
21. Xue, W. et al. Double-oxide sulfur host for advanced lithium-sulfur batteries. *Nano Energy* **38**, 12–18 (2017).
22. Li, S. et al. Developing high-performance lithium metal anode in liquid electrolytes: challenges and progress. *Adv. Mater.* **30**, 1706375 (2018).
23. Kushima, A. et al. Liquid cell transmission electron microscopy observation of lithium metal growth and dissolution: root growth, dead lithium and lithium flotsams. *Nano Energy* **32**, 271–279 (2017).
24. Xu, H. et al. Surpassing lithium metal rechargeable batteries with self-supporting Li–Sn–Sb foil anode. *Nano Energy* **74**, 104815 (2020).
25. Tatara, R. et al. Enhanced cycling performance of Ni-rich positive electrodes (NMC) in Li-ion batteries by reducing electrolyte free-solvent activity. *ACS Appl. Mater. Interfaces* **11**, 34973–34988 (2019).
26. Fan, X. et al. Highly fluorinated interphases enable high-voltage Li-metal batteries. *Chem* **4**, 174–185 (2018).
27. Chen, S. et al. High-voltage lithium-metal batteries enabled by localized high-concentration electrolytes. *Adv. Mater.* **30**, 1706102 (2018).
28. Fan, X. et al. All-temperature batteries enabled by fluorinated electrolytes with non-polar solvents. *Nat. Energy* **4**, 882–890 (2019).
29. Fan, X. et al. Non-flammable electrolyte enables Li-metal batteries with aggressive cathode chemistries. *Nat. Nanotechnol.* **13**, 715–722 (2018).
30. Cao, X. et al. Monolithic solid–electrolyte interphases formed in fluorinated orthoformate-based electrolytes minimize Li depletion and pulverization. *Nat. Energy* **4**, 796–805 (2019).
31. Yu, Z. et al. Molecular design for electrolyte solvents enabling energy-dense and long-cycling lithium metal batteries. *Nat. Energy* **5**, 526–533 (2020).
32. Zheng, Q. et al. A cyclic phosphate-based battery electrolyte for high voltage and safe operation. *Nat. Energy* **5**, 291–298 (2020).
33. Shyamsunder, A. et al. Inhibiting polysulfide shuttle in lithium–sulfur batteries through low-ion-pairing salts and a triflamide solvent. *Angew. Chem. Int. Ed.* **56**, 6192–6197 (2017).
34. Feng, S. et al. Molecular design of stable sulfamide- and sulfonamide-based electrolytes for aprotic $Li-O_2$ batteries. *Chem* **5**, 2630–2641 (2019).
35. Kim, U. H. et al. Microstructure-controlled Ni-rich cathode material by microscale compositional partition for next-generation electric vehicles. *Adv. Energy Mater.* **9**, 1803902 (2019).
36. Park, G.-T., Ryu, H.-H., Park, N.-Y., Yoon, C. S. & Sun, Y.-K. Tungsten doping for stabilization of $Li[Ni_{0.90}Co_{0.05}Mn_{0.05}]O_2$ cathode for Li-ion battery at high voltage. *J. Power Sources* **442**, 227242 (2019).
37. Eftekhari, A. Energy efficiency: a critically important but neglected factor in battery research. *Sustain. Energy Fuels* **1**, 2053–2060 (2017).
38. Pritzl, D., Solchenbach, S., Wetjen, M. & Gasteiger, H. A. Analysis of vinylene carbonate (VC) as additive in graphite/$LiNi_{0.5}Mn_{1.5}O_4$ cells. *J. Electrochem. Soc.* **164**, A2625–A2635 (2017).
39. Ma, T. et al. Revisiting the corrosion of the aluminum current collector in lithium-ion batteries. *J. Phys. Chem. Lett.* **8**, 1072–1077 (2017).
40. Sun, H.-H. & Manthiram, A. Impact of microcrack generation and surface degradation on a nickel-rich layered $Li[Ni_{0.9}Co_{0.05}Mn_{0.05}]O_2$ cathode for lithium-ion batteries. *Chem. Mater.* **29**, 8486–8493 (2017).
41. Liu, H. et al. Intergranular cracking as a major cause of long-term capacity fading of layered cathodes. *Nano Lett.* **17**, 3452–3457 (2017).
42. Li, W., Dolocan, A., Li, J., Xie, Q. & Manthiram, A. Ethylene carbonate-free electrolytes for high-nickel layered oxide cathodes in lithium-ion batteries. *Adv. Energy Mater.* **9**, 1901152 (2019).
43. Yan, P. et al. Tailoring grain boundary structures and chemistry of Ni-rich layered cathodes for enhanced cycle stability of lithium-ion batteries. *Nat. Energy* **3**, 600–605 (2018).
44. Kim, J. et al. Controllable solid electrolyte interphase in nickel-rich cathodes by an electrochemical rearrangement for stable lithium-ion batteries. *Adv. Mater.* **30**, 1704309 (2018).
45. Cha, H. et al. Boosting reaction homogeneity in high-energy lithium-ion battery cathode materials. *Adv. Mater.* **32**, 2003040 (2020).
46. Zhang, F. et al. Surface regulation enables high stability of single-crystal lithium-ion cathodes at high voltage. *Nat. Commun.* **11**, 3050 (2020).
47. Friedrich, F. et al. Capacity fading mechanisms of NCM-811 cathodes in lithium-ion batteries studied by X-ray diffraction and other diagnostics. *J. Electrochem. Soc.* **166**, A3760–A3774 (2019).
48. Xu, R., Sun, H., de Vasconcelos, L. S. & Zhao, K. Mechanical and structural degradation of $LiNi_xMn_yCo_zO_2$ cathode in Li-ion batteries: an experimental study. *J. Electrochem. Soc.* **164**, A3333–A3341 (2017).
49. Yao, Y.-X. et al. Regulating interfacial chemistry in lithium-ion batteries by a weakly-solvating electrolyte. *Angew. Chem. Int. Ed.* **60**, 4090–4097 (2020).
50. Yu, Y. et al. Coupled $LiPF_6$ decomposition and carbonate dehydrogenation enhanced by highly covalent metal oxides in high-energy Li-ion batteries. *J. Phys. Chem. C* **122**, 27368–27382 (2018).
51. Wolf, M., May, B. M. & Cabana, J. Visualization of electrochemical reactions in battery materials with X-ray microscopy and mapping. *Chem. Mater.* **29**, 3347–3362 (2017).
52. Yu, Y. et al. Revealing electronic signatures of lattice oxygen redox in lithium ruthenates and implications for high-energy Li-ion battery material designs. *Chem. Mater.* **31**, 7864–7876 (2019).
53. Evans, J., Vincent, C. A. & Bruce, P. G. Electrochemical measurement of transference numbers in polymer electrolytes. *Polymer* **28**, 2324–2328 (1987).

## Acknowledgements

## Author contributions

W.X., Y.D., J.A.J., Y.S.-H. and J. Li conceived the concept and the project. M.H., W.Z. and S.L. synthesized the solvent. W.X. designed the electrolyte and conducted electrochemical measurements. Y.L. conducted TOF-SIMS measurements and analysed the results. Y.G.Z. conducted in situ DEMS measurements. R.G. conducted focused ion beam and TEM analysis. W.X., X.X., D.Y., Z.S., C-J.S., I.H. and W.-K.L. conducted in situ synchrotron-based FXI measurements and analysed the results. P.L. conducted ICP-MS measurements. W.X., G.X., J. Lopez, W.F. and R.X. conducted other characterizations. W.X., Y.D., Y.Y., Y.S.-H, J.A.J. and J. Li wrote and revised the manuscript. All authors discussed the results and reviewed the manuscript.

## Competing interests

The authors declare no competing interests.